
10

Longwave Radiative Transfer in Inhomogeneous Cloud Layers

Robert G. Ellingson and Ezra E. Takara

10.1 Introduction	477
10.2 Models for Thermal Radiative Transfer Calculations	481
10.3 Overcast/clear linear mixing	483
10.4 Analytical Results for 3D Clouds	488
10.5 Monte Carlo Calculations for 3D Clouds	498
10.6 Summary	506
References	507

10.1 Introduction

The solar energy absorbed by the Earth-atmosphere system is balanced in the long term by radiant loss of energy by the system to space in the thermal infrared. The manner by which this loss to space occurs involves absorption, scattering and thermal emission by the surface and the gaseous and suspended matter (i.e., clouds and aerosols) within the atmosphere. These complex processes in the thermal infrared comprise the “atmospheric greenhouse effect,” which makes the Earth’s surface warmer than it would be if the atmosphere were not present and leads to a complex vertical temperature profile.

The Earth-atmosphere thermal radiative processes are non-linear in atmospheric properties, and there are complex radiation-climate feed back mechanisms. Furthermore, unlike solar radiation, thermal radiative processes occur continuously in time. Thus, realistic modeling of the climate system, as well as remote sensing techniques to accurately infer properties of the atmosphere, require accurate models of the various radiative processes that occur in the thermal infrared.

When absorption, thermal emission and scattering occur, the equation of radiative transfer under local thermodynamic equilibrium may be written as (see Chap. 3)

$$\begin{aligned} \boldsymbol{\Omega} \bullet \nabla I = & -\sigma_e(\mathbf{x})I(\mathbf{x}, \boldsymbol{\Omega}) \\ & + \sigma_s(\mathbf{x}) \int_{4\pi} p(\mathbf{x}, \boldsymbol{\Omega}' \rightarrow \boldsymbol{\Omega})I(\mathbf{x}, \boldsymbol{\Omega}')d\boldsymbol{\Omega}' + \sigma_a(\mathbf{x})B_v(T(\mathbf{x})) \end{aligned} \quad (10.1)$$

where σ_e , σ_s , and σ_a are the transport coefficients for extinction, scattering, and absorption respectively. Here, $\sigma_e = \sigma_s + \sigma_a$ and p is scattering phase function (normalized in such a way that its integral over 4π steradians is unity); ϖ_0 , the albedo of single scattering, is defined as the ratio of σ_s to σ_e . Finally, B_v is the Planck function depending on local temperature T , an isotropic source term. Neglecting incident solar radiation in the longwave portion of the spectrum (wavelength $\lambda \gtrsim 3\mu\text{m}$), solutions of this equation for the entire atmosphere are usually sought by assuming as boundary conditions zero incident radiation at the top of the atmosphere (TOA), and thermal emission and reflected incident radiation at the base. The effects of the solar longwave radiation, if important, are typically calculated separately, by means discussed in previous chapters. For downward flux considerations, this term is typically the order of 10 Wm^{-2} , on the order of a few percent of the thermal longwave flux incident on the surface.

When only gases are considered, ϖ_0 is essentially 0 in the thermal infrared due to the λ^{-4} decrease of the molecular scattering coefficient. For this case, the radiation field depends only on the absorption properties, amounts and distributions of the active gases, the temperature distribution, and the emission properties of the underlying surface. Due to the relative opacity of the atmosphere and the generally slow horizontal variation of temperature and absorbing gases, clear-sky radiation calculations are generally performed assuming a horizontally homogeneous atmosphere.

The main difference in the treatment of shortwave and longwave radiation is due to the spectral absorption of atmospheric gases. Figure 10.1 is a low-resolution depiction of the major absorption features of the dominant active gases and the approximate spectral distributions of incoming solar energy and terrestrial radiation emitted by the atmosphere. In the solar portion of the spectrum ($\lambda \lesssim 4\mu\text{m}$), there is little gaseous absorption across large regions of the spectrum, particularly the region from 0.3 to $1\mu\text{m}$, a region containing more than 50% of the incident solar radiation. This region is particularly sensitive to the presence of clouds since ϖ_0 for cloud particles is close to 1, and thermal emission by the gases is practically 0.

In the longwave, the atmosphere as a whole is nearly opaque to energy incident on its boundaries due to the strong vibration-rotation bands of H_2O , CO_2 , O_3 , CH_4 and N_2O . The major exception is the interval from 8 to $12\mu\text{m}$ or 1250 to 833 cm^{-1} (wavenumber in cm^{-1} is 10^4 times the reciprocal of wavelength λ in μm and vice-versa). Spectral intervals of significant transmission (lower absorption) are called windows. The primary window is the 8– $12\mu\text{m}$ interval; this is where clouds and 3D radiative transfer have their largest effects. There is also a “dirty” window centered near 500 cm^{-1} ($20\mu\text{m}$) which becomes significant in dry atmospheres.

The temperature variation in the atmosphere is relatively small, so there is little contrast between the incident and emitted radiation. Scattering effects are most pronounced when the emission source is at a much higher temperature than the scattering medium as in the shortwave. Therefore, scattering is much less significant in

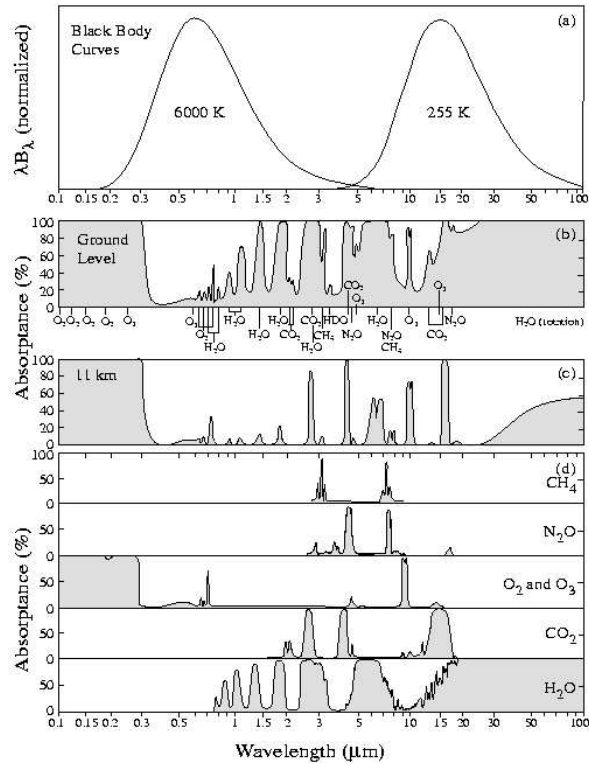


Fig. 10.1. (a) Planck function curves for approximate solar and terrestrial temperatures. (b) Absorption spectra for the entire vertical extent of the atmosphere. (c) Absorption spectra for the atmosphere above 11 km. (d) Atmospheric absorption spectra for the major active gases. From Thomas and Stamnes (1999), with permission.

the longwave than the shortwave. Because the gas concentrations, temperature and pressure vary with altitude, not every part of the atmosphere is opaque, and radiative transfer calculations are complicated by the structure of molecular line absorption.

The longwave optical properties of water clouds, shown in Fig. 10.2, are not nearly as spectrally detailed as those of the gases. ϖ_0 and extinction cross-sections vary strongly with particle size, but for typical cloud particle sizes, $\varpi_0 \approx 0.5$. However, the ϖ_0 to be used in calculations is that for the cloud-air mixture. Although cloud particles have non-zero scattering albedo across the longwave spectrum, the strong absorption by water vapor and other atmospheric gases reduces the effectiveness of scattering by cloud particles in the longwave compared to the shortwave. This is true even in the 8–12 μm window region, where the H_2O continuum absorbs a significant amount in humid atmospheres. Longwave 3D cloud scattering effects are reduced in those portions of the atmosphere where there is strong gaseous absorption.

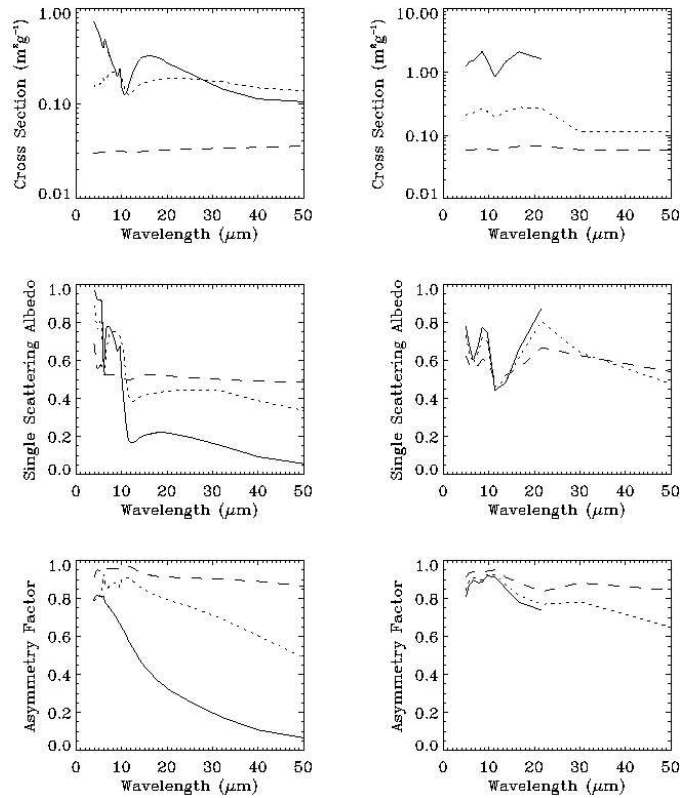


Fig. 10.2. Dependence of the cloud particle longwave optical properties on wavelength and effective radius, from Thomas and Stamnes (1999) with permission. The three left panels pertain to water clouds and the right panels to ice clouds. The curves in the left panels pertain to different effective cloud droplet radii; solid 3 μm ; dotted 10 μm ; dashed line 50 μm . The right panel curves correspond to different ice particle effective diameters; solid 6 μm ; dotted 25 μm ; dashed 100 μm .

As a result, 3D scattering effects are typically unimportant in climate models. The exception to this is for conditions typical of some cirrus clouds—thin cold clouds with large particles at low pressures where the concentrations of water vapor and the pressure broadening effects on line absorption are relatively small compared to the lower troposphere. Also, 3D scattering effects may be important for more detailed models such as cloud resolving models (CRMs) and large eddy simulations (LESs). Even in those cases, the spectroscopy of atmospheric gases plays a very large role in longwave 3D radiative transfer.

Although 3D cloud effects are potentially important for a variety of problems in remote sensing and climate studies, the discussion in this chapter is focused toward

climate applications. In the material that follows we summarize information on the calculation of radiation quantities for a two dimensional, horizontally homogeneous atmosphere. Next, longwave Monte Carlo calculations are introduced with some results expanding on the two dimensional calculations and results for a 3D calculation.

10.2 Models for Thermal Radiative Transfer Calculations

It is virtually impossible to describe the calculation details necessary to account for the spectroscopy of the longwave active gases and cloud particles in a review chapter such as this. Instead, only a verbal summary of the techniques is provided. Readers are urged to consult any of the referenced texts and journal articles for the important details.

Climate modelers are only interested in the spectrally integrated fluxes and heating rates. Unfortunately, the mathematical formalism developed with the monochromatic solutions is not transferable to frequency-averaged radiation. Furthermore, modelers are generally interested in effects of quantities over large spatial domains. The challenge of developing models for climate applications is to find solutions to (10.1) that adequately account for frequency variations as well as the spatial variations of the radiative fields.

The major obstacle for frequency integration of (10.1) is the spectral detail of gaseous absorption. Absorption features are composed of many discrete quantized events that are broadened due to collisions and/or thermal motions of the molecules. The discontinuous nature of these absorption features prohibits analytical solutions without approximations. As noted in Fig. 10.2, cloud particles and other aerosols have relatively slowly varying spectral absorption features. Outside of homogeneous spherical particles, however, our knowledge of cloud and aerosol radiative properties is still in its infancy. This is especially true for suspended ice particles. Furthermore, the horizontal and vertical distributions of clouds fall into a seemingly infinite range of possibilities, thereby precluding easy solutions.

Most climate models tend to determine fluxes and cooling rates by transforming the general three-dimensional radiative transfer problem into one-dimension. This is usually done by taking the average of clear and overcast quantities weighted by cloud amount(s). For example, the upward or downward flux of radiation F at a given level above or below a cloud layer is often calculated in climate models as

$$F = (1 - A_c)F_{\text{clear}} + A_c F_{\text{overcast}} \quad (10.2)$$

where F_{clear} and F_{overcast} are the fluxes calculated assuming homogeneous clear and overcast conditions respectively, and A_c is the cloud fraction. A more detailed discussion of (10.2) is provided in Sect. 10.4. Note that F_{clear} includes the effects of absorption and thermal emission by the atmospheric gases and non-cloud aerosols. F_{overcast} includes the simultaneous effects of clouds and gases.

Techniques for calculating radiative transfer are most easily classified according to the methods employed to perform the spectral integration of the gaseous absorption features, namely line-by-line (LBL) models and Band Models. Calculations in

LBL models are performed monochromatically, and they often include all of the detailed physics, including multiple scattering. Generally, these techniques offer the possibility of performing all of the numerics with high accuracy. They are particularly useful for checking the approximations made in less detailed models.

However, LBL models require substantial computing resources. For example, the thermal infrared portion of the spectrum may require the order of 10^7 intervals for monochromatic computations. Such computations were prohibitively expensive until the advent of supercomputers, but they are now relatively easy to do on desktop workstations. Furthermore, it is now possible to perform such calculations for a wide variety of atmospheric gases because of the wide distribution of tabulated values of the line strengths and half-widths important for line absorption. These models are very useful for remote sensing applications, but they consume too much computer time to be used in climate models.

Models for spectrally integrated gaseous absorption (i.e., band models) offer the possibility of rapid, but accurate, evaluation of the integral over detailed gas absorption spectra. The common approach used in band models is to make assumptions concerning the spectral distribution of absorption features for a homogeneous path that allow a solution in terms of analytical functions with a few adjustable parameters. The values of the adjustable parameters are specified either through fitting to more detailed model calculations or to asymptotic limits expressed in terms of line strengths and half-widths. Such models are applied to the inhomogeneous atmospheric path through a variety of scaling approximations developed from asymptotic solutions or linear expansions (e.g., the Curtis-Godson approximation). Excellent discussion of such techniques may be found in Goody and Yung (1989) and Liou (1980).

The analytical models take on a variety of forms and spectral resolution. Typically, those with spectral resolution less than about 50 cm^{-1} are called narrow band models, and those for larger intervals being labeled as wide band models. There has been a general assumption that the smaller the spectral interval, the more accurate the result. However, the results of the Intercomparison of Radiation Codes Used in Climate Models (ICRCCM; Ellingson and Fouquart, 1991) do not substantiate that position.

In an attempt to surmount the problem of arbitrary assumptions concerning the properties of analytic models, there have been several attempts to develop tabular values from LBL calculations. Such approaches increase numerical accuracy and speed at the expense of storage allocation, which is not a crucial consideration for current computers. The tabulations can be used to improve band models; but band models have a serious limitation: it is difficult to use them for problems involving multiple scattering. In monochromatic radiation the transmittance between two levels can be computed by multiplying the transmittances of sub-intervals. But this does not hold for band transmittances of the same gas, which are averaged over spectral intervals.

To avoid this problem, modelers have developed what is commonly called the k -distribution technique (see also Chap. 9). This technique transforms the integral over frequency to one over absorption coefficient. This is based on the observation

that the intensity is the same when the absorption coefficient is the same for a narrow spectral interval. Thus, the frequency integration is reduced to a sum of monochromatic problems. This approach requires the probability or cumulative probability distribution of absorption coefficients that may be determined numerically from LBL calculations or analytically from some band models. The k -distribution technique is not without limitations, because approximations must be made for application to the inhomogeneous atmosphere, and one may be required to keep large numbers of k 's for applications at low pressures (i.e., above about 20 km).

In summary, it must be remembered that band models are approximations and unwanted errors may occur unexpectedly. Some general statements concerning such models are: their absolute accuracy is only as good as that of the more detailed models or data on which they are based; fits based on asymptotic limits may be inaccurate for atmospheric calculations; accounting for overlapping absorption by two or more gases may be difficult for large band areas; application of scaling approximations are inaccurate in some situations; and except for the k -distribution, they are difficult to use in problems involving multiple scattering.

Parameterizations of the absorption by cloud particles typically express the wavenumber averaged transmittance through a cloud for a given direction in terms of the average cloud optical depth τ for the interval under consideration and the cosine of the local zenith angle μ as

$$\mathcal{T}(\tau; \mu) = e^{-\tau/\mu}.$$

For a given spectral interval, τ is the product of an effective radius dependent mass absorption coefficient (in $\text{m}^2 \text{g}^{-1}$) and liquid water path. For the $10 \mu\text{m}$ window region, the upper panel of Fig. 10.2 shows mass absorption coefficients are about 0.15 and $0.1 \text{ m}^2 \text{g}^{-1}$ for typical water and ice clouds, respectively. For liquid water contents of 0.1 g m^{-3} , typical of cumulus clouds, a 300 m deep cloud has an optical depth of about 4.5 —opaque although not black. As discussed below, cloud opacity extends over a wide range, with cirrus clouds tending to be the most transparent, and cumulus clouds the most opaque.

10.3 Overcast/clear linear mixing

To illustrate the bulk spectral effects of gaseous and cloud absorption and thermal emission, Fig. 10.3 shows the spectral distribution of the nadir (a) and zenith (b) radiances at the top and bottom of the atmosphere, respectively, with spectrally black clouds at different levels for mid-latitude summer (MLS) conditions calculated with a detailed band model. When the cloud level is at the surface (294 K), the downwelling radiance at the surface is the same as the Planck function for the temperature of the surface, whereas the upwelling radiance at the top is the same as for clear skies with a black surface. The TOA clear-sky upwelling radiance shows that outside of the $833\text{--}1250 \text{ cm}^{-1}$ window, the radiance originates at different levels of the atmosphere depending upon the opacity of the given spectral region. As the cloud

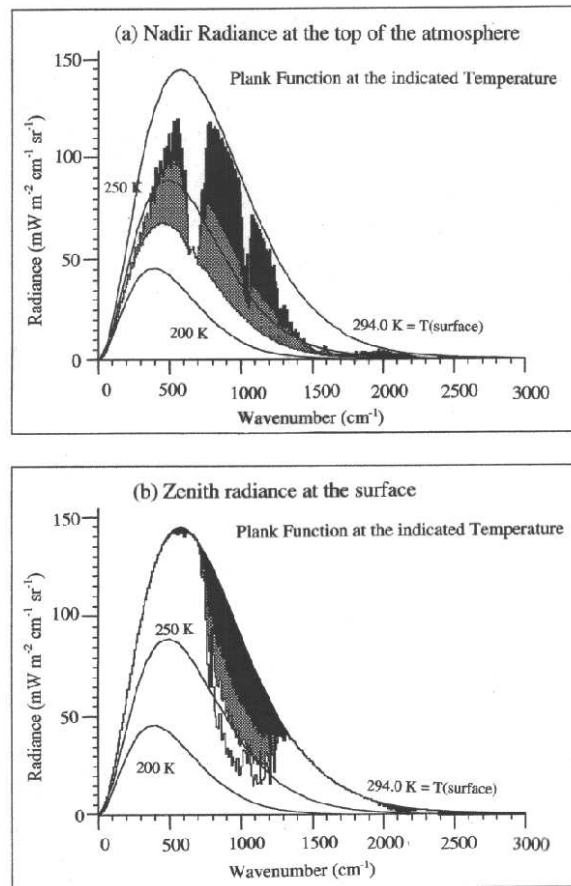


Fig. 10.3. Nadir (a) and zenith (b) radiances at the top and bottom of the atmosphere, respectively, for the Air Force Geophysical Laboratory (AFGL) mid-latitude summer (MLS) atmosphere calculated with the model of Warner and Ellingson (2000). The solid and hashed regions correspond to the change of the respective radiances resulting from increasing the altitude of a black plane parallel cloud from the surface to 4 km, and from 4 to 11 km, respectively. Note that the uppermost curve in (a) and the lowermost curve in (b) correspond to the clear-sky radiances.

level increases from the surface to 4 km, the TOA window region radiance follows the Planck function of the cloud temperature (250 K), whereas the remainder of the spectrum changes little, except for the 500 cm^{-1} “dirty” window. This occurs because the absorption features of the atmospheric gases outside of the window regions are large enough, even with the decreased absorption path, to block emission from the 4 km level. When the cloud reaches 11 km, the atmosphere above the clouds is

sufficiently transparent for the radiance to closely follow the Planck function of the assumed black cloud, except for the strongest regions of the 667 cm^{-1} ($15\text{ }\mu\text{m}$) CO_2 and 1042 cm^{-1} ($9.6\text{ }\mu\text{m}$) O_3 bands.

Except for the very driest atmospheres, the atmosphere is very opaque across the longwave spectrum, so the clear-sky downwelling radiance at the surface resembles the Planck function at the surface temperature. As stated in Sect. 10.1, the primary window is at $833\text{--}1250\text{ cm}^{-1}$ within this window surface emission can transmit directly to space. For drier atmospheres the 500 cm^{-1} “dirty window” can also transmit to space. Clouds effectively block these windows. As the cloud’s base altitude increases, two factors decrease its effect on downwelling at the surface. First, the cloud becomes colder. Second, the distance between the cloud and surface increases, increasing the amount of the atmosphere that can absorb emission from the cloud. When the cloud reaches 11 km, the overcast radiance distribution resembles the clear-sky radiance distribution.

In general, cloud effects on the downwelling radiance primarily occur in the $833\text{--}1250\text{ cm}^{-1}$ window, whereas for the TOA radiance, clouds dominate the window only when clouds are above about 4 km. When the clouds are above 4 km, the TOA radiance is affected by cloud absorption and scattering properties across the entire spectrum because of the decreased water vapor concentration. This shows quite dramatically that ice clouds can influence a large portion of the spectrum. Recall that scattering effects are most important when there is a significant temperature difference between the emission source and the scattering medium, as in the shortwave. Since ice clouds have the greatest temperature difference with the surface, their scattering can be important when they are located in colder regions of the atmosphere.

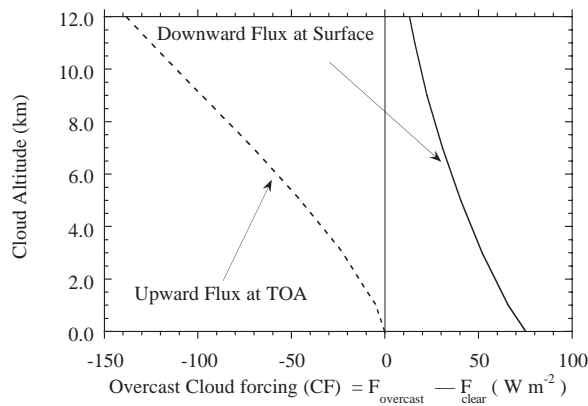


Fig. 10.4. Longwave black cloud forcing CF for overcast conditions at the top of the atmosphere (dashed) and surface (solid) as a function of cloud altitude for MLS conditions as calculated with the model of Warner and Ellingson (2000).

As previously discussed, cloud forcing is an important concept in climate studies. It is informative to examine it in the longwave. Cloud forcing (denoted CF) is defined as $CF = F - F_{\text{clear}}$, at the TOA and the surface. From (10.2), we obtain $CF = A_c(F_{\text{overcast}} - F_{\text{clear}})$. Figure 10.4 shows CF/A_c at the TOA and the surface for overcast black clouds at different levels. Note that the effects of non-blackness may be calculated for plane parallel clouds by multiplying A_c by the plane parallel cloud flux emissivity, ε_{cpp} given as

$$\varepsilon_{\text{cpp}} = 2 \int_0^1 (1 - e^{-\tau/\mu}) \mu d\mu = 1 - 2E_3(\tau) \quad (10.3)$$

where E_3 is the third-order exponential integral. Note that the effect of the variations of $A_c \varepsilon_{\text{cpp}}$ (hereafter denoted A_c^*) at a given cloud level (δA_c^*) is simply $\delta A_c^*(F_{\text{overcast}} - F_{\text{clear}})$.

For $A_c^* = 1$, the magnitude of TOA CF increases as the cloud altitude increases, whereas that for the surface decreases, both in accord with the expectations from Fig. 10.3. As clouds become more transparent, the magnitude of CF decreases for all cloud altitudes. Note however, that relatively small uncertainties in A_c^* yield large errors in CF . At the surface, a 15% error in A_c^* for a cloud at 0.5 km yields about a 10 Wm^{-2} uncertainty in the surface CF , whereas there is little change at the TOA. Such systematic, potentially global, 3D cloud effects are missing in current climate model simulations, leaving the possibility of significant climatic importance.

Cloud effects on the radiation field away from the boundaries of the atmosphere are more difficult to quantify in a simple fashion. Instead of looking at the flux field, it is more informative to examine the altitude and spectral distributions of the radiative cooling rate—the divergence of the net flux (Fig. 10.5). The clear-sky tropospheric distributions occur because cooling to space primarily controls the cooling rate. At a given wavenumber the maximum longwave cooling to space in an atmosphere with temperature decreasing with altitude occurs at optical depth 1. If the optical depth is less than 1, the maximum occurs in the layer closest to the surface. This occurs because of the near exponential decreases with height of the absorbing/emitting gas concentrations. At low altitudes the emission is high, but there is large attenuation. At high altitudes, the density is low, and there is less emission and attenuation. Thus, for clear-sky conditions, cooling in the lower troposphere is dominated by the atmospheric window where the optical depth is less than 1. As altitude increases, the very strong H_2O pure rotation band controls cooling. Since the optical depth varies with wavenumber, the altitude of maximum cooling shifts to the altitude where the optical depth equals 1.

The temperature gradient changes sign at the tropopause (near 13 km for the MLS sounding) and the cooling to space scenario is altered. In this sounding the heating in the 667 cm^{-1} region near 13 km is a result of the thermal emission by the very strong CO_2 band at the cold tropopause being less than the absorption from warmer layers nearby. The heating in the 10–20 km range in the 1000 to 1100 cm^{-1} region is due to the emission by O_3 being less than the absorption of relatively un-attenuated radiation from the lower troposphere.

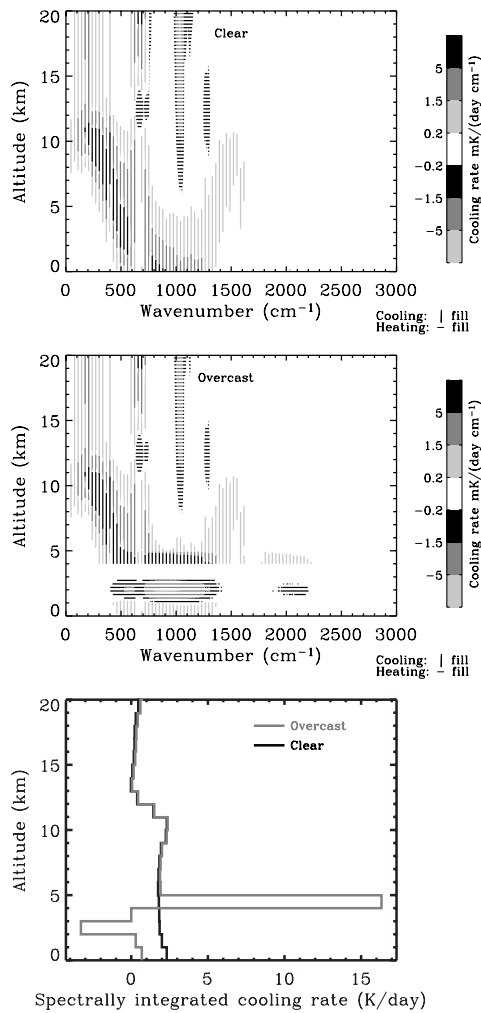


Fig. 10.5. Spectral distributions of longwave clear-sky (upper) and black overcast (lower) cooling rates for MLS conditions as calculated with the model of Warner and Ellingson (2000). The spectrally integrated cooling rates for these conditions are noted on the inserted middle figure. Clouds are assumed for the layer at 3–4 km.

When a cloud layer is added to the atmosphere (here for simplicity a black cloud in the 3-4 km layer), the cooling rate distribution changes dramatically in the vicinity of the cloud layer. Heating occurs immediately below the cloud layer due to absorp-

tion by the cloud of radiation from the more transparent regions. As expected, there is very little change at altitudes where the gaseous opacity is large. No cooling occurs in the assumed black cloud layer. There is strong cooling in the immediate layer above the clouds in the window regions, again related to the strong gradient in the cloud opacity. Within a couple of km of the cloud top, the cooling rate profile becomes almost identical to the clear-sky one as the local distribution of atmospheric opacity governs the cooling. Note that there is less heating by ozone due to the decreased radiation incident on the stratosphere when clouds are present. Also note that the higher a cloud is placed in the atmosphere, the larger the spectral range over which it is effective.

The earlier discussion for the cloud forcing may also be applied to the cooling rate. That is, uncertainties in the cloud fraction A_c^* lead to uncertainties in the cooling rate proportional to δA_c^* and the difference between the overcast and clear-sky cooling rates. For the clouds shown in Fig. 10.5, a 0.15 uncertainty in A_c^* results in about a $2.4^\circ\text{K day}^{-1}$ error in the cooling rate in the 1 km layer above the cloud, a number larger than the clear-sky cooling rate. The magnitude of the effects depends primarily upon the cloud location. As shown below, some longwave 3D effects yield uncertainties in A_c^* that will result in very large cooling rate errors. Since the general effect of longwave cooling is to destabilize the atmosphere by heating below the clouds and cooling above, uncertainties caused by neglecting 3D cloud effects in dynamical models will change the dynamics by virtue of a modified heating rate profile.

10.4 Analytical Results for 3D Clouds

Atmospheric modelers have typically reduced the 3D longwave cloud problem to a solution based on one-dimensional models by a series of assumptions concerning cloud properties. Consider the following assumptions:

- the molecular atmosphere is plane parallel and horizontally homogeneous;
- the cloud field for a given area is statistically homogeneous and isotropic.

Now determine the average flux for an area large compared to the individual cloud elements by summing separately the contributions of those solid angles that are completely clear and those that have cloud contributions. With these assumptions and with no scattering or ground reflection, the equation for the area-averaged downward flux at an altitude z below the clouds may be written as

$$\begin{aligned}
 F(z) = & 2\pi \int_0^{\pi/2} I_{\text{clear}}(z, \theta) P(\theta) \cos \theta \sin \theta d\theta \\
 & + 2\pi \int_0^{\pi/2} I_{\text{cloudy}}(z, \theta) [1 - P(\theta)] \cos \theta \sin \theta d\theta
 \end{aligned}
 \tag{10.4}$$

where $P(\theta)$ is the azimuthally-averaged probability of a clear line of sight (PCL) through the clouds at zenith angle θ , and I_{clear} and I_{cloudy} are the average radiant intensities from the clear and cloudy areas of the sky, respectively. Here it is assumed that the PCL $P(z, \theta) \equiv P(\theta)$ which is true at least for cloudy layers with vertical cloud boundaries.

Note that the above assumptions are only simplifying if it is possible to specify $P(\theta)$ and the area-averaged clear and cloudy sky radiances. For the clear-sky component, this is not a major concern barring frontal boundaries and orography, since the clear-sky radiative properties are quasi-horizontally homogeneous over large length scales. Clouds present more of a challenge because cloud field and radiance properties require major simplifications before $P(\theta)$ and I_{cloudy} can be determined. Furthermore, there are sparse observations or calculations with which to test the approximations.

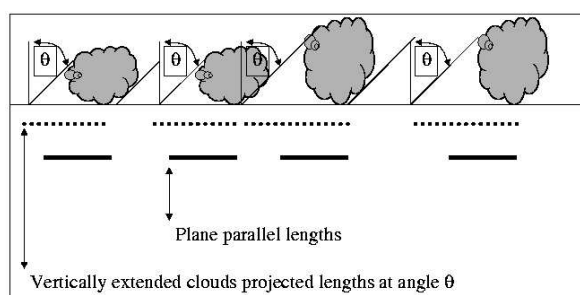


Fig. 10.6. Two dimensional view of an array of vertically extended clouds each with the same width. When viewed at angle θ , the clouds project as the dotted lines. When projected vertically downward, the cloud project as the solid horizontal lines (displaced here to coincide with the start of the dashed lines). The plane parallel cloud assumption, the solid lines, underestimates cloud cover at all view angles > 0 .

Figure 10.6 illustrates the overall geometrical effects of broken cloudiness. For illustration purposes, the clouds shown have the same horizontal lengths, but they have different vertical dimensions and irregular spacing. In this 2D transect, each cloud projects the same length at the level of cloud base from all view angles if only the cloud horizontal dimension is considered. Note that for very thin, randomly dispersed thin plates, $P(\theta)$ is $(1 - A_c)$, where A_c is the absolute cloud fraction. Assuming the thin plate clouds have identical radiative properties, (10.4) reverts to the standard approximation (10.2) used in most climate models. Thus for all z ,

$$F_{\text{thin}}(z) = (1 - A_c)F_{\text{clear}}(z) + A_c F_{\text{overcast}}(z). \quad (10.5)$$

That is, the flux is simply the cloud amount weighted average between the clear and overcast fluxes, each of which can be calculated with plane parallel techniques.

Now consider the effects of the vertical dimensions of the clouds by examining the projections of the vertical faces of the clouds on the horizontal plane when viewed

at an angle θ . As shown, when clouds are broken and have vertical extent, they project a larger area than their bases, thereby obscuring a larger fraction of the sky at a given angle than do flat plates with the same horizontal dimensions. One might anticipate that the effects of the vertical dimension to become larger as the clouds become tall relative to their bases. As will be seen below, when the cloud fraction is small, the clouds tend not to obscure one another. However, as fractional coverage of the bases increases, cloud sides become less important as mutual obscuration increases, a feature also connected with the distribution of cloud spacing. Additionally, since clouds are not isothermal, temperature variations along their sides must be accounted for in calculations.

Note that if the clouds have any depth, one cannot define an appropriate cloud fraction without also requiring the average fluxes to be dependent on the cloud properties. For example, if we define a hemispherically averaged cloud fraction A_{cH} as

$$A_{\text{cH}} = 2 \int_0^{\pi/2} [1 - P(\theta)] \sin \theta \cos \theta d\theta \quad (10.6)$$

and write the average flux as

$$\bar{F}(z) = (1 - A_{\text{cH}})\bar{F}_{\text{clear}}(z) + A_{\text{cH}}\bar{F}_{\text{cloudy}}(z). \quad (10.7)$$

This will require the average fluxes to be defined as

$$\bar{F}_{\text{clear}}(z) = \frac{2\pi}{(1 - A_{\text{cH}})} \int_0^{\pi/2} P(\theta) I_{\text{clear}}(z, \theta) \sin \theta \cos \theta d\theta \quad (10.8)$$

and

$$\bar{F}_{\text{cloudy}}(z) = \frac{2\pi}{A_{\text{cH}}} \int_0^{\pi/2} [1 - P(\theta)] I_{\text{cloudy}}(z, \theta) \sin \theta \cos \theta d\theta. \quad (10.9)$$

That is, the effective cloud fraction and the radiation field cannot be determined independently of each other.

10.4.1 Effective Cloud Fraction and Probability of Clear Line of Sight

The suggested reading contains references to many attempts that have been made to determine the form of $P(\theta)$ by making assumptions concerning the cloud field and the geometry of the individual cloud elements. In general, the approaches allow the equations for the upward and downward area-averaged fluxes to be written as

$$F = (1 - A_{\text{ce}})F_{\text{clear}} + A_{\text{ce}}F_{\text{overcast}} \quad (10.10)$$

where A_{ce} is an effective cloud fraction that depends upon the assumptions made concerning the cloud field, F_{clear} is the clear-sky flux calculated with the domain-averaged clear-air radiative properties, F_{overcast} is the flux calculated for overcast conditions with assumed cloud radiative properties. The advantage of this approach is that

it allows climate codes to use their radiation models with new parameterizations of A_{ce} . However, it must be remembered that none of these attempts have included the effects of scattering between broken cloud elements or have been shown conclusively to account adequately for all three-dimensional cloud effects.

Many of the bulk geometrical effects of clouds on $P(\theta)$ may be appreciated by considering an array of identical right-circular cylinders of thickness H , radius R , and cloud positions distributed according to a Poisson distribution with areal density parameter γ . For such an array, $P(\theta)$ may be written as (Avaste et al., 1974)

$$P(\theta) = \exp[-\gamma(\pi R^2 + 2HR \tan \theta)]. \tag{10.11}$$

Note that the terms in parentheses are simply the areas of a cloud base and the side, respectively projected onto the base level. $P(\theta)$ is a maximum when looking directly overhead ($\theta = 0$) and goes to 0 when looking at the horizon ($\theta = \pi/2$).

Defining the absolute cloud amount as $1 - P(0)$, allows $P(\theta)$ to be written as

$$P(\theta) = (1 - A_c) \exp(b \tan \theta) \tag{10.12}$$

where

$$b = 2\beta \ln(1 - A_c) / \pi,$$

and β , the aspect ratio, is H/R .

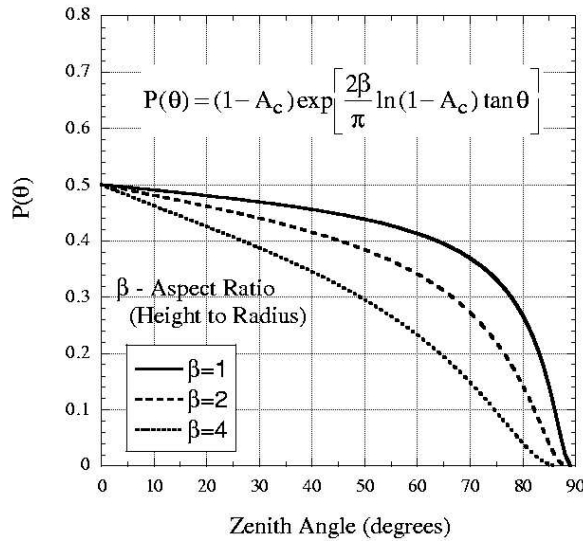


Fig. 10.7. Probability of a clear line of sight $P(\theta)$ for a random cylindrical cloud field as a function of zenith angle for 50% absolute cloud cover A_c and different aspect ratios β .

Figure 10.7 illustrates $P(\theta)$ as a function of θ for a few different aspect ratios for 50% absolute cloud cover. $P(\theta)$ decreases with increasing θ and β , since more cloud

side areas are seen at a given θ . Note that the horizon is not visible for these type clouds.

Note that even with the simple form of (10.12), it is easily seen that A_{ce} cannot be separated from the radiance fields without further assumptions. However, due to the quasi-isotropic nature of the radiance fields, the angular integration poses no major computational problem. For an isotropic radiance assumption and for isothermal black clouds, A_{ce} is easily shown to be a function of A_c and β given by

$$A_{ce} = A_c + (1 - A_c) \left[1 - 2 \int_0^{\pi/2} \exp(b \tan \theta) \sin \theta \cos \theta d\theta \right]. \quad (10.13)$$

Thus, A_{ce} is always $> A_c$, and varies with A_c in a complex fashion dependent upon β .

10.4.2 Geometrical Effects of Broken “Black” Clouds

Despite some of the shortcomings of such simplifications for the properties of the cloud and radiance fields, it is illustrative to examine the results from at least one model to glean the overall bulk 3D geometrical effects, sans scattering. The results shown herein draw heavily from the work of Han and Ellingson (1999) that assumes truncated square pyramids, a critical nearest neighbor spacing of clouds, and power law distributions for both cloud size and spatial distributions. Clouds are assumed to be spectrally black, a good assumption for cumulus clouds with optical thickness greater than 3—a few hundred meters thick. Since we wish to highlight the effects relative to the thin plate approximation, results are shown as $A_{ce} - A_c$. This combined with the results shown in Fig. 10.4 provides a useful method for estimating the possible flux errors inherent in neglecting cloud geometry.

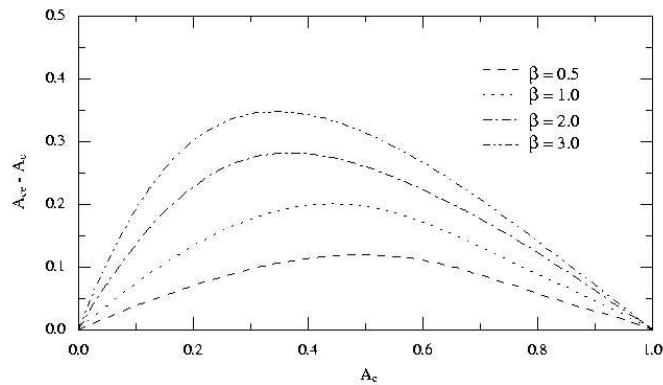


Fig. 10.8. $A_{ce} - A_c$ as a function of A_c and β on A_{ce} for isothermal cylindrical clouds.

Figure 10.8 shows $A_{ce} - A_c$ as a function of A_c for isothermal cylindrical clouds for different aspect ratios, assuming realistic values for cloud spacing and sizes. Note that the larger β , the larger the cloud side area relative to base area. When A_c is small, mutual shading is not significant and cloud sides make a large contribution to A_{ce} .

The error in neglecting cloud geometry can be estimated by combining the results shown in Figs. 10.4 and 10.8. Since the cumulus clouds depths are approximately the same as their widths; $\beta \approx 2$. From Fig. 10.8 the error for $\beta = 2$ peaks at $A_c \approx 0.35$; $A_{ce} - A_c \approx 0.275$. From Fig. 10.4 the overcast cloud forcing at the surface for cloud altitude 0.5 km is approximately 70 Wm^{-2} . To get the forcing for fractional cloudiness, multiply by A_{ce} to account for cloud geometry. Multiplying by A_c neglects cloud geometry. In this case, $(A_{ce} - A_c)CF \approx 20 \text{ Wm}^{-2}$; neglecting cloud geometry will underestimate the downward flux at the surface by 20 Wm^{-2} .

Non-isothermal clouds in an atmosphere with temperature decreasing with increasing altitude have smaller bulk geometry effects, because the cloud sides are closer to the clear-sky radiance field. If the clouds are tall enough so that the flux from top to bottom increased by a factor of two, the maximum effect would decrease by about 30%.

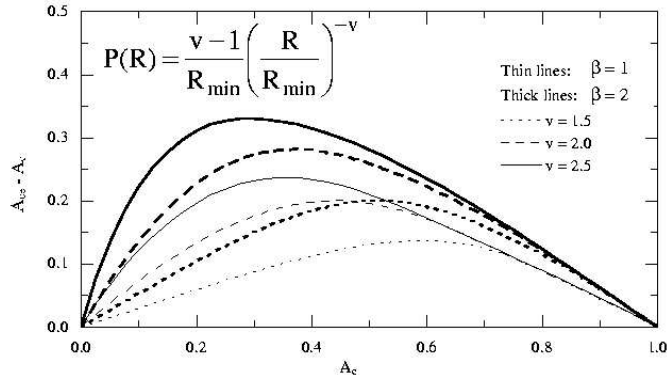


Fig. 10.9. The effects of size distribution exponent ν on A_{ce} for different β . $P(R)dR$ is the probability of a cloud of size R and $R + dR$. A larger ν implies a larger number of clouds of the same cloud size. For low A_c , the spatial distances remain large. More clouds tend to offer a greater area of cloud sides and a greater A_{ce} .

The effects of varying the exponent ν of an assumed power law distribution of cloud sizes are shown in Fig. 10.9. A larger ν implies a larger number of clouds of the same cloud size. For low A_c , the spatial distances remain large. More clouds tend to offer a greater area of cloud sides and a greater A_{ce} . Nonetheless, it is quite clear that the geometrical effects can be reduced by about 50% and moved to larger cloud fractions by having a wider spread in the sizes of the clouds. Note that ν is not a routinely observed quantity or one that is predicted by climate models.

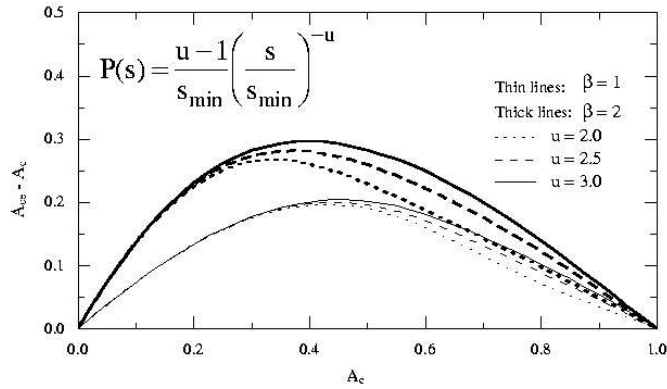


Fig. 10.10. The effects of spatial distribution exponent u on A_{ce} . $P(s)ds$ is the probability of spacing between s and $s + ds$; $u > 1$. When u is large, clouds are more sparsely distributed and cloud sides tend to be obscured less and generate a larger A_{ce} .

The effects of varying the exponent u of an assumed power law distribution of cloud spacing are shown in Fig. 10.10. When u is large, clouds are more sparsely distributed and cloud sides tend to be obscured less and generate a larger A_{ce} . Note that the major effects of spacing become more apparent for A_c between 0.4 and 0.7, and tend to be about 25% of the effects caused by realistic variations in the cloud size distributions.

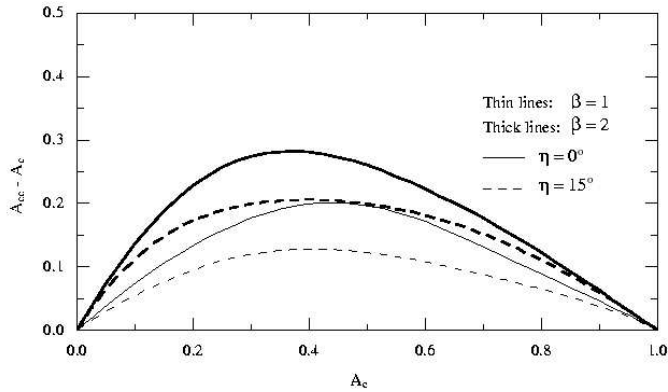


Fig. 10.11. The effect of side inclination η on the effective cloud fraction for different β .

The inclination of cloud sides is also important, as this reduces the area of the projected sizes (see Fig. 10.11). A modest change in the site inclination ($\eta = 15^\circ$) reduces the maximum geometric effect by about 33% over a broad range of A_c . Al-

though not shown, the effects of different cloud shapes are realized primarily through the inclination factor.

It is not at all clear which if any of the geometrical models represent real clouds, because few observational studies have been performed, and there are conflicting results from those that have been performed. Figure 10.12 show the results of an attempt to compare observed with model calculated values of $A_{ce} - A_c$ for relatively thick, single layer cumulus clouds. In general, the observations show the same general trend of different models, but there are few observations in the range of parameter space where the models are most sensitive.

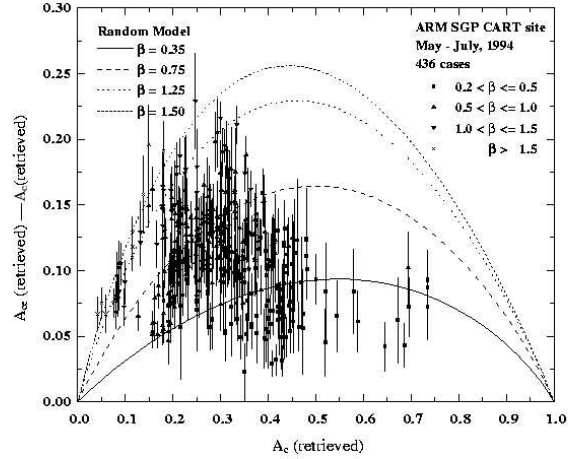


Fig. 10.12. The distribution of $A_{ce} - A_c$ as functions of A_c and β from 436 cases of single-layer cumulus clouds observed in 1994 at the ARM site in Oklahoma, USA. Half of each vertical bar indicates the standard deviation of uncertainty in the retrieved A_{ce} . The curves are from a model assuming random cylinders. Data are from Han (1999).

10.4.3 Heterogeneous Non Black Clouds

As noted in Sect. 10.3, for non-black plates of uniform optical thickness, A_c in (10.2) is replaced by the product of A_c and the plane-parallel cloud flux emissivity,

$$\varepsilon_{\text{cpp}}(\tau) = 1 - 2E_3(\tau),$$

where τ is the cloud optical depth E_3 is the third-order exponential integral, and F_{overcast} is replaced by $F_{\text{overcast}}(\text{black})$, the flux resulting from a black cloud; that is,

$$F = (1 - A_c \varepsilon_{\text{cpp}}(\tau)) F_{\text{clear}} + A_c \varepsilon_{\text{cpp}}(\tau) F_{\text{overcast}}(\text{black}). \quad (10.14)$$

There is large body of literature on analysis of observations that find a wide range of optical depths for liquid water clouds, even for marine stratocumulus cloud fields

that appear to be horizontally homogeneous. Due to the highly non-linear dependence of the cloud emissivity on τ for moderate τ , it is important to consider the appropriate average $\bar{\epsilon}$ rather than ϵ at the average τ .

To illustrate the potential effects of the horizontal distribution of optical depth, assume that in our domain, the cloud radiance at a given level and zenith angle, $I_{\text{cloudy}}(z, \theta)$ at any position in the domain under consideration varies from other positions due only to the cloud absorption optical depth τ viewed at θ . We'll neglect the possibility that a given view actually intersects more than one cloud. Consider probability distributions of τ for lines of sight along θ , and denote these probability densities of τ , conditional on θ , as $P(\tau|\theta)$.

Assuming $P(\theta)$ and $P(\tau|\theta)$ independent allows us to write the domain averaged cloudy sky radiance $\bar{I}_{\text{cloudy}}(z, \theta)$ as

$$\bar{I}_{\text{cloudy}}(z, \theta) = \int_0^{\infty} P(\tau|\theta) I_{\text{cloudy}}(z, \theta, \tau) d\tau. \tag{10.15}$$

Assume now that the clouds are isothermal and that the monochromatic cloud emission $I_{\text{cloudy}}(z, \theta, \tau)$ be approximated as $[1 - e^{-\tau \sec \theta}] B_{\text{vc}}$ where B_{vc} is the Planck function for the temperature of the cloud. For illustration purposes, the appropriate domain averaged monochromatic emissivity ϵ_{ca} for vertically extended clouds is then given as

$$\epsilon_{\text{ca}} = 2 \int_0^{\infty} d\tau \int_0^{\pi/2} P(\tau|\theta) [1 - e^{-\tau \sec \theta}] \cos \theta \sin \theta d\theta. \tag{10.16}$$

Recent observational studies of marine stratocumulus with high resolution Landsat data by Barker and Wielicki (1997) have shown that the 1000 cm^{-1} ($10 \mu\text{m}$) window region optical depth is represented well by the Gamma distribution written as

$$P_{\Gamma}(\tau) = \frac{1}{\Gamma(\nu)} \left(\frac{\nu}{\bar{\tau}}\right)^{\nu} \tau^{\nu-1} e^{-\nu\tau/\bar{\tau}}; \tau > 0, \nu > 0 \tag{10.17}$$

where $\Gamma(\nu)$ is the Gamma function, irrespective of θ . The parameter ν is given by $(\bar{\tau}/\sigma)^2$, where σ is the standard deviation of the distribution of τ with mean $\bar{\tau}$.

With this definition of $p(\tau)$, Barker and Wielicki derive a cloud emissivity $\epsilon_{c\Gamma}$ using (10.16) and (10.17) to obtain

$$\begin{aligned} \epsilon_{c\Gamma}(\bar{\tau}) = 1 - \frac{1}{\Gamma(\nu)} \left(\frac{\nu}{\bar{\tau}}\right)^{\nu} \left\{ \left(\frac{\bar{\tau}}{\nu + \bar{\tau}}\right)^{\nu} \left[\Gamma(\nu) - \frac{\bar{\tau}}{\nu + \bar{\tau}} \Gamma(\nu + 1) \right] \right. \\ \left. + \int_0^{\infty} E_1(\tau) \tau^{\nu+1} e^{-\nu\tau/\bar{\tau}} d\tau \right\} \end{aligned} \tag{10.18}$$

where E_1 is the first-order exponential integral.

It should be noted that (10.18) holds strictly for monochromatic radiation. However, since the liquid water optical properties vary slowly with wavenumber in the

thermal infrared, this form might be used for the spectrally averaged flux transmittance.

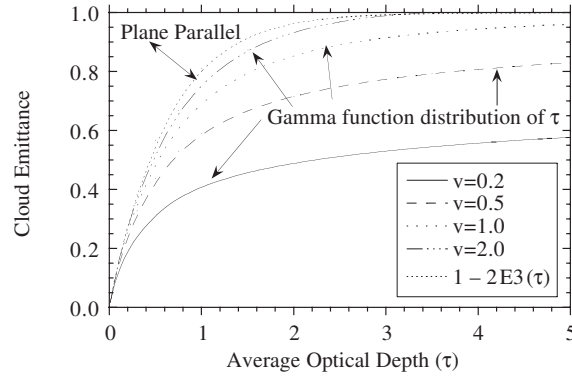


Fig. 10.13. Comparison of ε_{cpp} (dotted) and $\varepsilon_{\text{c}\Gamma}$ as a function of average cloud optical depth for different Gamma distributions of optical depth as embodied in parameter ν .

Figure 10.13 shows $\varepsilon_{\text{c}\Gamma}$ and the ε_{cpp} for a range of ν and τ . For $\nu \lesssim 2$, $\varepsilon_{\text{c}\Gamma}$ depends markedly on ν , and $\varepsilon_{\text{c}\Gamma} < \varepsilon_{\text{cpp}}$ for all τ . Note that for $\tau > 3$, $\varepsilon_{\text{cpp}} > \varepsilon_{\text{c}\Gamma}$ by more than a factor of 2 for $\nu = 2$, an observed set of parameters. For $\tau \approx 1$, a value representative of relatively thin stratocumulus, $\varepsilon_{\text{cpp}} \approx 0.8$, whereas $\varepsilon_{\text{c}\Gamma}$ varies between about 0.40 for $\nu = 0.2$ to 0.75 for $\nu = 2$. Clearly, horizontal variations of τ are important.

Note that the effects of variations in τ on the downward flux at the surface are dramatic for low-level clouds. For overcast conditions typical of stratocumulus, the plane parallel black cloud approximation would be about 35 Wm^{-2} greater than values computed with $\varepsilon_{\text{c}\Gamma}(\tau = 3, \nu = 0.2)$. For 50% cloud cover with cumuli with aspect ratios ≈ 1 , the flat plate approximation would be 20 Wm^{-2} greater than the combined effects of geometry and optical depth variability. Incorporating the cloud geometry alone exceeds the combined effects by 35 Wm^{-2} . Clearly, neglecting optical depth variability can lead to significant flux errors.

The relative sensitivity of the flux to the combined effects of geometry and optical depth variability, with respect to the flat plate approximation, may be written as

$$\frac{\delta F}{F_{\text{overcast}} - F_{\text{clear}}} \approx \frac{A_{\text{ce}} - A_{\text{c}}}{A_{\text{ce}}} + \frac{\varepsilon_{\text{c}\Gamma} - \varepsilon_{\text{cpp}}}{\varepsilon_{\text{c}\Gamma}}. \quad (10.19)$$

Assuming the $P(\theta)$ and $p(\tau|\theta)$ given herein are approximately correct when $\nu \gtrsim 2$, cloud geometrical effects dominate for all τ . Note that non blackness is an important consideration for those cases with $\tau \lesssim 3$. For $\nu \lesssim 0.5$ and all τ , variations in τ will dominate. For other values of τ and ν , the effects of cloud geometry and optical depth variability may well be of similar magnitude but of opposite sign,

depending upon the values of various parameters. Additional observations and/or numerical modeling are necessary to ascertain the atmospheric conditions controlling the importance of geometry and optical depth variability.

10.5 Monte Carlo Calculations for 3D Clouds

In the longwave, the Monte Carlo method is nearly identical with the shortwave. Tracking photon bundles through probabilistic transmission, absorption, and scattering events simulates the radiative transfer. The only difference is source of the photon bundles—in the longwave, the surface, cloud elements, and the atmospheric gases are emitters. Any simulation must account for these emission sources.

For a diffuse surface, the emission zenith angle is

$$\theta = \cos^{-1} \sqrt{\alpha} \quad (10.20a)$$

while for a volumetric emitter, such as a gaseous or cloud element,

$$\theta = \cos^{-1}(1 - 2\alpha); \quad (10.20b)$$

in both cases, the emission azimuth angle is

$$\phi = 2\pi\alpha. \quad (10.20c)$$

Here, α denotes independently generated random numbers uniformly distributed between 0 and 1. The above simulation rules follow directly from the simulation of continuous random variables with a given probability density function described in Sect. 4.2.2. For example, for diffuse surface, probability density function is $P(\theta) = \sin 2\theta$, $0 \leq \theta < \pi/2$; thus (10.20a) follows directly from (4.33)–(4.34).

10.5.1 Forward vs. Backward Monte Carlo

As described in Sect. 4.2, forward and backward Monte Carlo algorithms have advantages and disadvantages. These are more pronounced in the longwave since every element of the atmosphere and the surface emits in the longwave.

Because the emitting temperatures are almost the same, it is common to emit the same number of photons from each element and normalize the fractions according to the temperature and optical properties. A more sophisticated method is to use the temperature and optical properties to partition the photon bundles among the emitting elements. The fractional probability of being emitted by the i th surface element, f_{si} at temperature T_i and a wavenumber interval centered on ν is

$$f_{si} = \frac{\pi \int_{A_i} \varepsilon_{\nu i} B_{\nu}(T_i) dA_i}{U} \quad (10.21a)$$

$\varepsilon_{\nu i}$ is the emissivity of surface element i ; A_i is the area of element i ; B_{ν} is the Planck function at wavenumber ν . Similarly, the fractional probability of being emitted by

the i th volumetric (gaseous and cloud) element, $f_{\nu i}$ at temperature T_i and a wavenumber interval centered on ν is

$$f_{\nu i} = \frac{\pi \int_{V_i} a_{\nu i} B_{\nu}(T_i) dV_i}{U} \quad (10.21b)$$

$a_{\nu i}$ is the absorptivity of volumetric element i ; V_i is the volume of element i . U is the sum of all emitted energy at wavenumber ν over the M surface elements and N volumetric elements:

$$U = \pi \sum_{i=1}^M \int_{A_i} \varepsilon_{\nu i} B_{\nu}(T_i) dA_i + \pi \sum_{i=1}^N \int_{V_i} a_{\nu i} B_{\nu}(T_i) dV_i. \quad (10.21c)$$

The primary disadvantage of forward Monte Carlo arises when only a limited number of quantities need to be computed and there are a large number of emitting elements, such as for remote sensing. In that case a large number of the tracked photon bundles will not contribute to the solutions; energy partitioning as in (10.21a-c) will reduce this problem.

Backwards Monte Carlo is advantageous when the number of computed quantities are small compared to the number of emitting elements. When the computed quantities are roughly equal in number and location as the emitting elements, the methods are equivalent. If there are more computed quantities than emitting elements, forward Monte Carlo is more efficient.

Parallel computing is an obvious path to improve the speed of Monte Carlo calculations. Since each photon bundle is independent, Monte Carlo is readily adapted to parallel computing. Backwards Monte Carlo can be directly implemented; the backward tracking origin points can be spread among the processors and the results gathered at the end. This requires minimal communication between processors, a single number (the answer) can be passed. Forward Monte Carlo requires more communication. Like the backward calculation, the bundle tracking from emission point can be spread among the processors. To compute the quantities the statistics from each emission point must be gathered together. Gathering the statistics requires passing arrays instead of single numbers. Unlike the serial case, it is not clear which method has the advantage in a given situation.

10.5.2 Quasi-3D Example

In Sect. 10.4.2 we used analytical solutions for broken black clouds. Non-black and scattering clouds were not examined because they greatly increased the complexity. However, the Monte Carlo method can easily use the probability of clear line sight expressions and account for cloud transmission and scattering. For example, a single layer cloud field composed of homogenous cylinders with random horizontal overlap as in Takara and Ellingson (2000). To emphasize the cloud geometry and scattering, consider only the 833–1250 cm^{-1} atmospheric window.

The upward and downward fluxes are found through a spectral and angular integration of radiances,

$$F^{\uparrow\downarrow} = \int_0^{\pi/2} I^{\uparrow\downarrow}(\theta) \cos(\theta) d\theta = \sum_{j=1}^3 w_j I^{\uparrow\downarrow}(\theta_j). \quad (10.22)$$

The w_j are the Gaussian weights for the Gaussian angles in the interval $0 < \theta < \pi/2$. Here a 3-point quadrature is used. The upward and downward radiances, $I^{\uparrow\downarrow}$, are computed by summing over the wavenumber intervals:

$$I^{\uparrow\downarrow} = \int_{833 \text{ cm}^{-1}}^{1250 \text{ cm}^{-1}} I_v^{\uparrow\downarrow} dv = \sum_{i=1}^6 I_i^{\uparrow\downarrow} \Delta v_i. \quad (10.23)$$

Here, $I_i^{\uparrow\downarrow}$ is the spectral radiance or specific intensity of the i th wavenumber interval. The intervals (in cm^{-1}) are: $833 < v_1 < 909 < v_2 < 1000 < v_3 < 1081 < v_4 < 1143 < v_5 < 1212 < v_6 < 1250$.

Outside the cloud layer, the radiances are computed using the transmission and emission calculated using a line-by-line radiative transfer model (or “LBLRTM”) assuming a black surface. Backward Monte Carlo simulations are used to find the radiances emerging from the cloud layer; to find the emerging radiance at Gaussian angle θ_j , bundles are emitted into the layer at $(\pi - \theta_j)$. Using the PCL it is determined whether or not bundles intersected a cloud element. For random number α ,

$$\begin{cases} \alpha \leq \text{PCL: bundle does not intersect clouds} \\ \alpha > \text{PCL: bundle intersects clouds} \end{cases} \quad (10.24)$$

The transmissivity is computed throughout the cloud layer at 25-meter intervals. Since transmissivities range between 0 and 1 they can be used directly to model transmission or absorption probabilities. For a bundle emitted at z_j traveling upward to z_i and random number α ,

$$\begin{cases} \alpha \leq T(z_i, z_j, \theta) : \text{ bundle is transmitted} \\ \alpha > T(z_i, z_j, \theta) : \text{ bundle is extinguished} \end{cases} \quad (10.25)$$

The bundle extinction location, z_{ext} , is found by equating the ratios of T and z :

$$\frac{\alpha - 1}{T(z_i, z_j, \theta) - 1} = \frac{z_{\text{ext}} - z_j}{z_i - z_j} \quad (10.26a)$$

where $T = 1$ corresponds to the emission point at z_j and $T(z_i, z_j, \theta)$ to the end of the path at z_i . This linear approximation assumes that each layer is optically thin. Solving for z_{ext} gives:

$$z_{\text{ext}} = z_j + \frac{z_i - z_j}{T(z_i, z_j, \theta) - 1} (\alpha - 1). \quad (10.26b)$$

The transmission from z_j traveling upward to z_i through the cloud is the product of gaseous and cloud transmission.

$$T(z_i, z_j, \theta) = T_{\text{gas}}(z_i, z_j, \theta) T_{\text{cloud}}(z_i, z_j, \theta) \quad (10.27a)$$

$$T_{\text{cloud}}(z_i, z_j, \theta) = \exp\left(-\frac{\tau}{\cos \theta}\right) = \exp[-\sigma_e \left(\frac{z_i - z_j}{\cos \theta}\right)] \quad (10.27b)$$

$$T(z_i, z_j, \theta) = T_{\text{gas}}(z_i, z_j, \theta) \exp[-\sigma_e \left(\frac{z_i - z_j}{\cos \theta}\right)] \quad (10.27c)$$

where σ_e is the extinction coefficient.

If the photon bundle is extinguished then it is either scattered or absorbed. The albedo of single scattering, ϖ_0 , determines which occurs. For random number α ,

$$\begin{cases} \alpha \leq \varpi_0 : & \text{bundle is scattered} \\ \alpha > \varpi_0 : & \text{bundle is absorbed} \end{cases} \quad (10.28)$$

There is no scattering for a bundle with a clear line of sight, $\varpi_0 = 0$, so the bundle is always absorbed. If the bundle is scattered, a new direction is assigned using the phase function through the same process described in Sect. 4.2.

Results are computed for the McClatchey tropical (TRP) and sub-arctic winter (SAW) soundings. A single layer of water clouds is inserted at three different cloud base altitudes (z_b), 0.5, 2, and 4 km. Within the clouds, an effective radius (r_e) of $5 \mu\text{m}$ is assumed for the droplets. The clouds are given two different geometries, large and small. For the large clouds, the aspect ratio (β) is 2 and the cloud diameter (D) is 1 km; the cloud thickness is 1 km. For the small clouds, $\beta = 1$ and $D = 0.25$ km; the cloud thickness is 0.125 km. The liquid water content (LWC) is 0.1 gm^{-3} for SAW and 1 gm^{-3} for TRP. For these LWC, the SAW small water cloud optical thickness is approximately 3 in the vertical direction, and 30 for the TRP.

To determine the relative importance of scattering and geometry for water clouds the results are compared to Monte Carlo computations with black clouds—the black cloud approximation. The bias error for the black cloud approximation is

$$\delta X = X(\text{approximation}) - X; \quad X = F^\uparrow, F^\downarrow. \quad (10.29)$$

In Fig. 10.14a (TRP) the absolute values of the errors are less than 0.9 Wm^{-2} , quite small. For water clouds the black cloud approximation works because the downward emission by the water clouds is augmented by the downward reflection of upward flux at the cloud bottom. This can be seen by noting that the error is negative at $A_c = 1$. Since the apparent cloud emission is greater than the blackbody emission, the apparent emissivity of the water cloud is larger than one. The high temperature and water vapor concentration in the first kilometer masks the scattering effect at the surface. This agrees with observational studies of cumulus cloud fields.

In Fig. 10.14b (SAW), the errors are less than 2 Wm^{-2} for the large clouds, and approaches 11 Wm^{-2} for small clouds. The small cloud errors decrease as cloud height increases, peaking at $A_c = 0.7$. Because the small clouds are not opaque, there is direct transmission from the surface to the upper atmosphere. The surface “sees” the cold upper atmosphere. Though the cloud bottom continues to reflect, a good deal of the surface radiation is transmitted through the clouds. The reflection

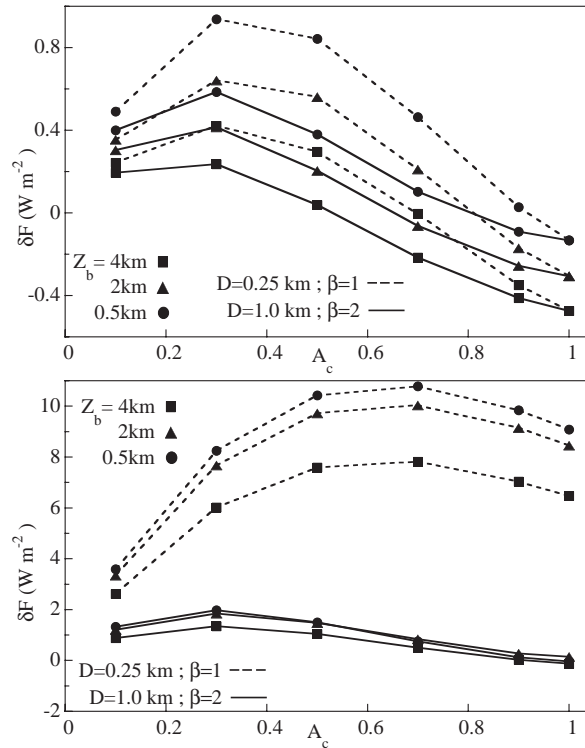


Fig. 10.14. (a) TRP downward flux error at surface for large and small water clouds at various z_b ; $\text{LWC} = 1\text{ g m}^{-3}$, $r_e = 5\text{ }\mu\text{m}$. (b) SAW downward flux error at surface for large and small water clouds at various z_b ; $\text{LWC} = 0.1\text{ g m}^{-3}$, $r_e = 5\text{ }\mu\text{m}$. Notice the vastly different ordinate scales.

from the cloud bottom is not large enough to compensate for the reduced emission, unlike Fig. 10.14a. As a result, the black cloud approximation fails. Since the small water cloud vertical optical thickness is approximately 3; this agrees with the results in Sect. 10.4.2 and results by Harshvardhan (1982).

The errors for the upward flux at 15 km are shown in Figs. 10.15a,b. In Fig. 10.15a (TRP), the absolute value of the error is less than 4 Wm^{-2} . The error increases almost linearly with A_c ; the larger clouds having more error than the smaller clouds. In this case, the black cloud approximation overestimates the flux above the clouds. The clouds are too opaque to allow transmission from the lower atmosphere. Scattering clouds trap their emissions within themselves; so the outward emission by the clouds is reduced. Unlike for surface fluxes, there is no reflection from the cloud top to compensate for the lower emission by the cloud. This effect is more noticeable above the thicker water clouds where atmospheric emission is reduced. Fig. 10.15b (SAW) also shows a similar pattern, except for the small water cloud at 4 km. From Fig. 10.14b,

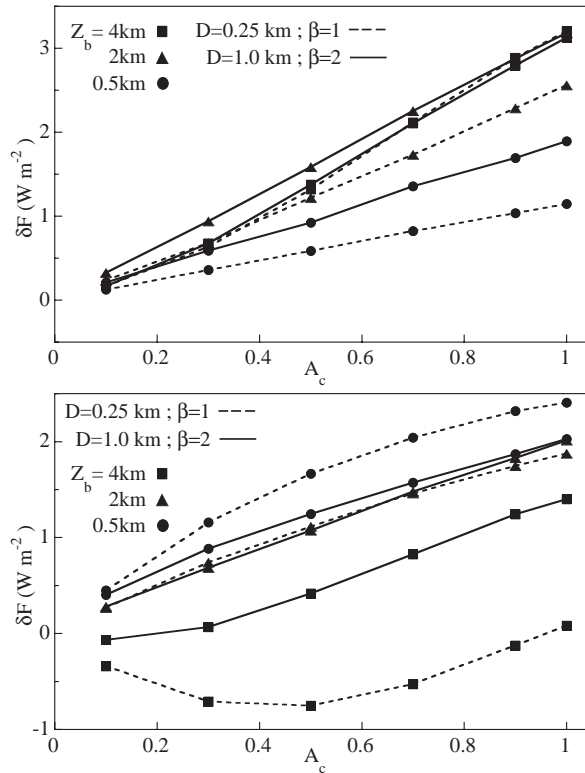


Fig. 10.15. (a) TRP upward flux error at 15 km for large and small water clouds at various z_b ; $LWC = 1 \text{ g m}^{-3}$, $r_c = 5 \mu\text{m}$. (b) SAW upward flux error at 15 km for large and small water clouds at various z_b ; $LWC = 0.1 \text{ g m}^{-3}$, $r_c = 5 \mu\text{m}$.

the small clouds are partially transparent and the large clouds are opaque. It might be expected that the small cloud errors would cluster together as in Fig. 10.14b. But only the small water cloud at 4 km stands apart. For the other clouds, the black cloud approximation overestimates the flux and the error increases almost linearly with A_c . Since the optical thickness of the small clouds is low enough to allow transmission while the large clouds are opaque, it is curious to see similar errors for large and small clouds at 0.5 and 2 km. The explanation is in the temperature profile. In this sounding, the temperature increases slightly with altitude for the first kilometer, drops back down at 2 km and remains almost the same up to 3 km. As a result, 0.5 and 2 km clouds (both large and small) are at almost the same temperature as the atmosphere below. Only the 4 km clouds are significantly colder than the lower atmosphere. Since the small cloud is partially transparent, the energy from the lower levels radiates through the cloud layer. This leads to an underestimation of the flux by the black cloud approximation.

In general the black cloud approximation worked well for opaque water clouds with flux errors less than 5 Wm^{-2} . When the cloud optical thickness is reduced, so that the cloud is no longer opaque, the black cloud approximation fails. The results indicate that individual cloud geometry is of primary importance for opaque water clouds. The errors due to neglecting cloud scattering are largest close to the cloud layer and decrease as the distance from the cloud layer increases. This reduction occurs most rapidly below 3 km. Since the effects of water cloud longwave scattering are effectively muted in the $833\text{--}1250 \text{ cm}^{-1}$ window, scattering effects from optically thick water clouds should not be significant over the longwave spectrum.

10.5.3 Fully-3D Example

The Intercomparison of Three-Dimensional Radiation Codes (I3RC) has provided excellent examples of three-dimensional cloud problems. The most computationally intensive is from an LES-based prediction of a cumulus field featuring a 100×100 grid in the horizontal with a vertical grid of 30 layers and periodic boundary conditions Fig. 10.16a.

Note that the fourth quadrant ($x > 3 \text{ km}$, $y < 3 \text{ km}$) is almost cloud free. The I3RC specified several problems for this simulated field, one of which is to find the surface downward flux at 1000 cm^{-1} for each grid point (10,000 points in all). The backward Monte Carlo computation used here assumed cells centered on each grid point with constant properties. Quantities are calculated at the midpoint or center point of each zone. The bundles are tracked from the middle or center of each cell.

Bundle tracking proceeded as in Sect. 10.5.2, i.e., (10.25) for transmission and (10.28) for scattering are directly applied. Since it is assumed that there is no horizontal variation in temperature it is not necessary to tabulate the horizontal components of the absorption locations, only the vertical locations are necessary. Once the bundle tracking is completed, the fractions accumulated in each vertical location can be used to compute the downward flux at the surface ($z = 0$) F^\downarrow :

$$F^\downarrow = \pi f_s B_v(T_s) + \pi \sum_{k=1}^{30} f_{vk} B_v(T_k) \quad (10.30a)$$

where subindex “s” stands for surface while “v” stands for volume. Here f_s is the ratio of the number of bundles that reach and are absorbed by the surface, N_s , to the total number of bundles emitted at the computation point, N :

$$f_s = \frac{N_s}{N} \quad (10.30b)$$

and f_{vk} is the same ratio for the number of bundles that reach and are absorbed in layer k , N_{vk} :

$$f_{vk} = \frac{N_{vk}}{N}. \quad (10.30c)$$

Note that the number of bundles that reach the TOA (set at $z = 30 \text{ km}$) is not tabulated since there is no downward emission from space (other than the longwave portion of the solar spectrum).

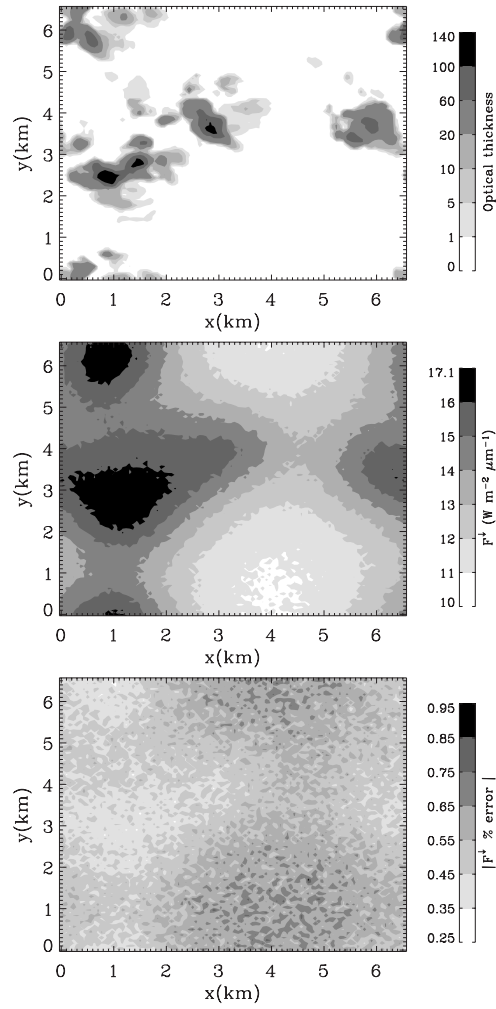


Fig. 10.16. (a) Column integrated optical thickness for I3RC cumulus field at 1000 cm^{-1} . (b) 1000 cm^{-1} downward flux at surface for I3RC cumulus field. (c) Percent Monte Carlo error estimate (absolute value) for 1000 cm^{-1} downward flux at surface for I3RC cumulus field.

To compute the upward flux at TOA F^{\uparrow} , photons are tracked backwards from the starting points at the top of the atmosphere.

$$F^\dagger = \pi f_s B_V(T_s) + \pi \sum_{k=1}^{30} f_{vk} B_V(T_k). \quad (10.31)$$

To compute q , the heating rate per unit volume at a particular point $(x, y, z)^T$, photons are tracked backwards from that point:

$$q = 4\pi\sigma_a \left[f_s B_V(T_s) + \sum_{k=1}^{30} f_{vk} B_V(T_k) \right] - 4\pi\sigma_a B_V(T) \quad (10.32)$$

where σ_a is the absorption coefficient and T is the temperature at position $(x, y, z)^T$, typically only a function of z . The first term is the absorbed energy per unit volume; $4\pi\sigma_a B_V(T)$ is the energy emitted per unit volume.

Fig. 10.16b is the downward surface spectral $10\ \mu\text{m}$ flux for the 100×100 horizontal grid. The fluxes at each point are computed by backward tracking 10,000 bundles. Approximately 12 hours are needed to compute the 10,000 fluxes on an 800 Mhz Linux workstation. The three-dimensional effects of the clouds will be most apparent for this spectral flux since it is near the center of the $833\text{--}1250\ \text{cm}^{-1}$ window region. In Fig. 10.16b, the clear fourth quadrant from Fig. 10.16a is a region of low downward flux. The areas below the clouds have high downward flux. The estimated percentage numerical error (absolute value) estimate is shown Fig. 10.16c. The estimated error is under one percent throughout, indicating that 10,000 bundles from each surface mid-point will give a good estimate for the surface flux over the entire region. Note that the areas of lower error are below the clouds (high flux) and the higher errors are in the clear areas (low flux). The time required to compute these fluxes is a drawback of the Monte Carlo method and emphasizes the importance of carefully implementing a Monte Carlo calculation.

10.6 Summary

Within this chapter basic information on gas and cloud spectroscopy and an introduction to longwave calculations with results are presented. This is followed by analytical results for 3D clouds and then a discussion of longwave Monte Carlo with some results.

The discussion of spectroscopy in Section 10.1 shows that atmospheric gases are quite opaque. For clear skies, there are two spectral intervals with significant surface to TOA transmission: the primary $833\text{--}1250\ \text{cm}^{-1}$ ($8\text{--}12\ \mu\text{m}$) window and the “dirty” window $500\ \text{cm}^{-1}$ ($20\ \mu\text{m}$), which becomes significant in dry atmospheres. In comparison to the gaseous absorption which varies greatly within a small spectral interval the cloud radiative properties vary quite slowly. The introduction to longwave calculations in Sect. 10.2 and the results shown in Sect. 10.3 show the blocking effect of clouds in the primary $833\text{--}1250\ \text{cm}^{-1}$ window, which yields higher downwelling at the surface and lower upwelling at the TOA. Clouds affect the atmospheric cooling rate through the optical depth gradients at their boundaries. This results in

heating below the cloud layer and cooling above. In partially cloudy cases, a 15% error in plane parallel cloud fraction leads to very large cooling rate errors.

The analytical results for 3D clouds in Sect. 10.4 use the concept of the probability of a clear line of sight to generate analytical solutions for broken cloud fields of various size and space distributions. From this the effect of cloud geometry is determined. For the simple isothermal cylindrical cloud model, neglecting cloud geometry can lead to underestimating the downwelling flux at the surface by as much as 20 W m^{-2} . A more complex model featuring truncated square pyramids with power law distributions for cloud size and spacing generally agrees with measurements. The comparison of the effect of cloud non blackness to geometry shows that for clouds with large optical depth and low variability, cloud geometry is most important. For clouds with high variability in optical depth, the variability and non-blackness is most important. Sect. 10.5 describes aspects of the Monte Carlo method in the longwave; expressions for longwave emission and the relative merits of forward and backward Monte Carlo are described. Results from an extension of the work on analytical results for 3D clouds that includes scattering and transmission are presented. They show that in very humid atmospheres with opaque clouds, cloud scattering has very little effect on surface flux compared to the black cloud approximation. The high humidity masks out the scattering effect. Scattering does have an effect for the upward flux at 15 km; it lowers the emission from the cloud top. Lastly, surface fluxes for a full-blown monochromatic 3D Monte Carlo model are shown. The computation is quite lengthy for 10,000 bundles from each of the 10,000 computation points. Even with the vast increases in computer speed, long computational times are a problem for Monte Carlo calculations.

References

- Avaste, O.A., Y.R. Mullamaa, K.Y. Niylik, and M.A. Sulev (1974). On the coverage of sky by clouds. Technical Report Tech. Transl. TT-F-790 - Heat Transfer in the Atmosphere, NASA.
- Barker, H.W. and B.A. Wielicki (1997). Parameterizing grid-averaged longwave fluxes for inhomogenous marine boundary layer clouds. *J. Atmos. Sci.*, **54**, 2785–2798.
- Ellingson, R.G. and Y. Fouquart (1991). The intercomparison of radiation codes in climate models (ICRCCM): An overview. *J. Geophys. Res.*, **96**, 8925–8927.
- Goody, R.M. and Y.L. Yung (1989). *Atmospheric Radiation Theoretical Basis*. Oxford University Press, New York (NY).
- Han, D. (1999). *Studies of Longwave Radiative Transfer Under Broken Cloud Conditions: Cloud Parameterizations and Validations*. Ph.D. dissertation, University of Maryland, College Park, College Park (MD).
- Han, D. and R.G. Ellingson (1999). Cumulus cloud formulations for longwave radiation calculations. *J. Atmos. Sci.*, **56**, 837–851.
- Harshvardhan (1982). The effect of brokenness on cloud-climate sensitivity. *J. Atmos. Sci.*, **39**, 1853–1861.

- Liou, K.-N. (1980). *An Introduction to Atmospheric Radiation*. Harcourt Brace Jovanovich, San Diego (CA).
- Takara, E.E. and R.G. Ellingson (2000). Broken cloud field longwave scattering effects. *J. Atmos. Sci.*, **57**, 1298–1310.
- Thomas, G. and K. Stamnes (1999). *Radiative Transfer in the Atmosphere and Ocean*. Cambridge University Press, New York (NY).
- Warner, J. and R. Ellingson (2000). A new narrowband radiation model for water vapor absorption. *J. Atmos. Sci.*, **57**, 1481–1496.

Suggested Further Reading

- A. Benassi, F. Szczap, A.B. Davis, M. Masbou, C. Cornet and P. Bleuyard (2004). Thermal radiative fluxes through inhomogeneous cloud fields: A sensitivity study using a new stochastic cloud generator, *Atm. Res.*, **72**, 291–315.
- Cahalan, R.F. and J.H. Joseph (1989). Fractal statistics of cloud fields. *Mon. Wea. Rev.*, **117**, 261–272.
- Clough, S.A., F.X. Kneizys and R.W. Davies (1989). Line shape and the water vapor continuum. *Atm. Res.*, **23**, 229–241.
- Clough, S.A., M.J. Iacono and J.L. Moncet (1992). Line-by-line calculations of atmospheric fluxes and cooling rates: Application to water vapor. *J. Geophys. Res.*, **97**, 15761–5785.
- Ebert, E.E. and J.A. Curry (1992). A parameterization of ice cloud optical properties for climate models. *J. Geophys. Res.*, **97**, 3831–3836.
- Ellingson, R.G. and J.C. Gille (1978). An infrared transfer model. Part I: Model description and comparison of observations with calculations. *J. Atmos. Sci.*, **35**, 523–545.
- Ellingson, R.G. (1982). On the effects of cumulus dimensions on longwave irradiance and heating rates. *J. Atmos. Sci.*, **39**, 886–896.
- Ellingson, R.G., J. Ellis and S. Fels (1991). The intercomparison of radiation codes in climate models (ICRCCM): Longwave results. *J. Geophys. Res.*, **96**, 8929–8953.
- Fu, Q. and K.N. Liou (1993). Parameterization of the radiative properties of cirrus clouds. *J. Atmos. Sci.*, **50**, 2008–2025.
- Hu, Y.X. and K. Stamnes (1993). An accurate parameterization of the radiative properties of water clouds suitable for use in climate models. *J. Climate*, **6**, 728–742.
- Kauth, R.J. and J.L. Penquite (1967). The probability of clear lines of sight through a cloudy atmosphere. *J. Appl. Meteor.*, **6**, 1005–1017.
- Killen, R. and R.G. Ellingson (1994). The effects of shape and spatial distribution of cumulus clouds on longwave irradiance. *J. Atmos. Sci.*, **51**, 2123–2136.
- Niylik, K.Y. (1968). Atmospheric thermal radiation in partly cloudy regions. *Izv. Acad. Sci. USSR, Atmos. Oceanic Phys.*, **4**, 383–396.
- Plank, V.G. (1969). The size distribution of cumulus clouds in representative Florida populations. *J. Appl. Meteor.*, **8**, 46–67.

- Takara, E.E. and R.G. Ellingson (1996). Scattering effects on longwave fluxes in broken cloud fields. *J. Atmos. Sci.*, **53**, 1464–1476.
- Zhu, T., J. Lee, R.C. Weger and R.M. Welch (1992). Clustering, randomness, and regularity in cloud fields: 2. Cumulus cloud fields. *J. Geophys. Res.*, **97**, 20,537–20,558.